Available online at www.sciencedirect.com

SciVerse ScienceDirect

Ceramics International 39 (2013) 4113–4123

CERAMICS INTERNATIONAL

www.elsevier.com/locate/ceramint

Modeling of the performance of BSCF capillary membranes in four-end and three-end integration mode

C. Buysse[a,b], B. Michielsen[a,*], V. Middelkoop[a,b], F. Snijkers[a], A. Buekenhoudt[a], J. Kretzschmar[b], S. Lenaerts[b]

[a]*Flemish Institute for Technological Research—VITO, Boeretang 200, B-2400 Mol, Belgium*
[b]*Department of Bioscience Engineering, University of Antwerp, CGB, Groenenborgerlaan 171, B-2020 Antwerp, Belgium*

Received 30 August 2012; received in revised form 29 October 2012; accepted 30 October 2012
Available online 9 November 2012

Abstract

Owing to their high surface-to-volume ratio, there has been an increasing research interest in mixed ionic–electronic conducting (MIEC) capillary membranes for large-scale high temperature oxygen separation applications. They offer an energy-efficient solution for high temperature combustion processes in oxy-fuel and pre-combustion CO_2 capture technologies used in fossil fuel power plants. In order to assess the effectiveness of these membranes in power plant applications, the impact of the geometry of $Ba_{0.5}Sr_{0.5}Co_{0.8}Fe_{0.2}O_{3-\delta}$ (BSCF) capillaries on their performance in the three-end and four-end integration modes has been investigated and thoroughly discussed. The model's parameters were derived from four-end mode lab-scale experiments using gas-tight, macrovoid free and sulfur-free BSCF capillary membranes that were prepared by a phase-inversion spinning technique. The results of this modeling study revealed that in the four-end mode higher average oxygen fluxes and smaller total membrane areas can be obtained than in the three-end mode. This is due to the higher pO_2 gradient across the membrane wall.

Keywords: Modeling; MIEC capillary membranes; Four-end mode; Three-end mode

1. Introduction

Mixed ionic–electronic conducting (MIEC) perovskite membranes have been attracting significant research interest in recent years due to their potential application in oxy-fuel and pre-combustion CO_2 capture routes in fossil fuel power plants. Their capability to separate oxygen from air within high temperature combustion processes, has the potential to minimize the plant's efficiency losses to around 2–8% points [1–6]. If they are gas-tight, such membranes show 100% oxygen selectivity in the presence of an oxygen partial pressure gradient and at high temperatures (>700 °C) since only oxygen ions can travel through the oxygen vacancies of the crystal lattice from the high pO_2 side of the membrane to the low. At the same time, electrons travel in the opposite direction through the membrane to maintain charge neutrality, eliminating the need for electrodes and external electrical circuits [7–11]. A standard fossil fuel power plant with oxy-fuel or pre-combustion capture requires an oxygen flow rate of $\sim$8000 t per day [1,5]. Therefore, in order for the MIEC technology to be economically viable, both high oxygen fluxes and high surface-to-volume ratios need to be obtained. For power plant applications, an oxygen flux of 10 N ml cm^{-2} min^{-1} is postulated, limiting the total required membrane area to $\sim$38850 m^2 [12,13]. In theory, the capillary and hollow fiber geometry provide the largest membrane area in relation to the volume of the membrane module, potentially minimizing the required number of membranes in a module. For large-scale gas separation applications, capillaries and hollow fibers fulfill this requirement more adequately than flat sheet and tubular membranes. However, most modeling and design studies are performed with the latter type of geometries [14–21]. There is little data in the literature on the performance of MIEC capillaries and hollow fibers under

*Corresponding author. Tel.: +32 1433 5667; fax: +32 1432 1186.
E-mail address: bart.michielsen@vito.be (B. Michielsen).

0272-8842/$ - see front matter © 2012 Elsevier Ltd and Techna Group S.r.l. All rights reserved.
http://dx.doi.org/10.1016/j.ceramint.2012.10.266

Nomenclature

$J(O_2)_L$	local oxygen permeation flux (ml cm^{-2} min^{-1})	P_2	oxygen partial pressure at the permeate side (Pa)
$J(O_2)$	average oxygen permeation flux (ml cm^{-2} min^{-1})	l	length of the capillary (cm)
C_i	density of oxygen ions (m s^{-1})	S	effective membrane area of the capillary (m^2)
D_a	ambipolar oxygen ion-electron hole diffusion coefficient (m^2 s^{-1})	R_o	outer radius of the capillary (mm)
D	outer diameter of the capillary (mm)	R_{in}	inner radius of the capillary (mm)
d	inner diameter of the capillary (mm)	dP_T	total pressure drop on the permeate side of the capillary (Pa)
pO_2	oxygen partial pressure (Pa)	ρ	density of the gas mixture (kg m^{-3})
P_1	oxygen partial pressure at the feed side (Pa)	V	velocity of the gas mixture (m s^{-1})
		f	friction coefficient
		Re	Reynolds number

industrial working conditions. From a technological point of view, MIEC membranes can be integrated with fossil fuel power plants using a four-end or three-end integration mode [22,23]. In the four-end integration mode, CO_2 and H_2O rich flue gasses are typically used to sweep away the permeated oxygen. In the three-end mode, the permeated pure oxygen is drawn out by a vacuum pump, avoiding contact with the flue gasses [1,5,6,22]. $Ba_{0.5}Sr_{0.5}Co_{0.8}Fe_{0.2}O_{3-\delta}$ (BSCF), which has the potential to achieve the commercially interesting oxygen flux of 10 N ml cm^{-1} min^{-1}, is nowadays considered a first generation material and potential candidate for operation in a three-end design in oxy-fuel or precombustion processes, because BSCF membranes can only operate in the presence of an oxygen chemical potential gradient and at elevated temperatures [1,5,18,22,24]. Its instability in high CO_2 concentrations excludes the use of BSCF in the four-end integration mode. The gradual transformation from the cubic structure to the hexagonal, limits its use to temperatures above 850 °C [23,25–28].

The work herein reports the results of modeling studies to scope the impact of the geometry of MIEC capillaries (outer and inner diameter, membrane length) on their performance in both three-end and four-end modes with a view to their integration in fossil power plant processes. The model's parameters were derived from lab-scale experiments using gas-tight, macrovoid-free and sulfur-free BSCF capillary membranes with an outer diameter of ~3.6 mm and a wall thickness of 0.4 mm prepared by a phase-inversion spinning technique [29,30].

2. Experimental

2.1. Oxygen flux measurements through BSCF capillaries under four-end lab-scale conditions

Oxygen permeation fluxes through gas-tight, macrovoid-free and sulfur-free BSCF capillaries with a *ca.* 3.6 mm outer diameter and 0.4 mm wall thickness were studied as a function of temperature and argon (Ar) sweep gas flow rate at 750–950 °C using the experimental setup described in [29,31,32]. BSCF capillaries of about 3 cm in length were hermetically sealed between two gas-tight YSZ tubes in the hot zone of the furnace using high temperature glass so as to ensure isothermal conditions. The shell side of the capillary was fed with synthetic air (100 N ml min^{-1}). Argon, at a constant partial pressure of oxygen p(O_2) of 5×10^{-5} bar, was supplied to the core side of the capillary. The oxygen partial pressure in the sweep gas stream was measured by an electrochemical oxygen sensor attached to the outlet of the YSZ tube, allowing for the calculation of the average oxygen flux through the membrane. The flow rates at the inlet and outlet of the system were compared in order to confirm the gas-tightness of the glass seal.

2.2. Modeling assumptions

Fig. 1 is a sketch of a single MIEC capillary in the four-end and three-end operation modes. In power plants, increasing air compression and decreasing vacuum pressures, lead to an increase in energy demand allowing for high oxygen fluxes. In turn, the total membrane area required for oxygen production decreases. For these processes to be industrially viable they need to strike the right balance between total membrane cost and minimizing the efficiency penalty in case the membrane unit is integrated into a combustion power

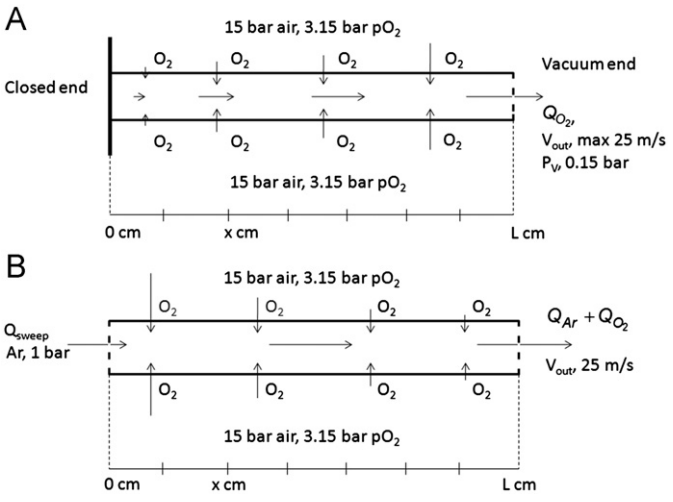

Fig. 1. Schematic drawing of a BSCF capillary in three-end mode (A) and four-end operation mode (B).

plant. With regards to the impact of turbo machinery on the integration of MIEC membranes in the three-end and four-end design and its potential for efficiency improvements, further details can be found in the literature [1,5,22].

An operating temperature of 850 °C was chosen, based on it being the minimum temperature at which the transformation from the cubic phase to the hexagonal phase of BSCF is prevented. The air feed pressure was set to 15 bar ($pO_2 = 3.15$ bar) which is comparable to the pressure used in cryogenic air distillation [33], while a low vacuum of 0.15 bar was used to keep the energy consumption of the vacuum pump to a minimum [34]. In the four-end mode, argon (total pressure = 1 bar, $pO_2 = 5 \times 10^{-5}$ bar) was used as sweep gas with the velocity of the hot gas leaving the capillary ($Ar + O_2$) fixed at 25 m s^{-1}. Higher velocities may lead to resonances which are detrimental to the membrane [33]. This same value was used as the maximum gas velocity leaving the core side of the capillary integrated in the three-end mode.

In formulating the mathematical models describing the oxygen flux through the capillary membranes, the following assumptions were made [35,36]:

- The mass transfer resistance of gaseous oxygen from the gas stream to the membrane surface (high pO_2 side) and from the membrane surface to the gas stream (low pO_2 side) are negligible. The pO_2 values at the membrane surfaces are therefore identical at the shell and core side.
- The ideal gas law is applied to describe gas behavior.
- Air composition and total air pressure along the outer surface of the capillary membrane (feed side) are constant.
- The system operates under steady-state isothermal conditions.
- Axial diffusion of gases is negligible.

As reported elsewhere, oxygen fluxes through 0.4 mm thick sulfur-free BSCF capillaries with an outer diameter of ~3.5 mm measured at 850–950 °C under four-end lab-scale conditions are found to be distinctly limited by bulk diffusion [26]. Drawing on this, the oxygen flux through the capillary membranes in both the three-end and four-end operation modes was modeled applying bulk-diffusion limitation.

2.3. Modeling of the oxygen permeation fluxes through MIEC capillaries in four-end and three-end integration

2.3.1. Four-end integration mode

The local oxygen permeation flux $j(O_2)_L$ limited by bulk diffusion through a MIEC capillary can be described as [36,37]:

$$j(O_2)_L = \frac{\pi C_i D_a}{2\ln(D/d)} \ln\left(\frac{P_1}{P_2}\right) \frac{dl}{dS} \quad (1)$$

where C_i is the density of oxygen ions, D_a the ambipolar oxygen ion–electron hole diffusion coefficient, D and d are the outer and inner diameter of the capillary, P_1 and P_2 are the oxygen partial pressures at the feed and permeate side of the membrane, respectively, l is the length of the capillary. The effective membrane area of the capillary, S is:

$$S = \frac{2\pi(R_o - R_{in})l}{\ln(R_o/R_{in})} \quad (2)$$

with R_o and R_{in} being the outer and inner radius of the capillary, respectively. Based on the assumptions made in the model previously described [35,36], the total pressure drop on the permeate side of the capillary dP_T over an infinitesimal length dl is given by:

$$dP_T = \frac{f\rho V^2}{2d} dl \quad (3)$$

where ρ is the density of the gas mixture, V is the velocity of the gas mixture, d is the inner diameter of the capillary and f is the friction coefficient:

$$f = \frac{64}{\mathrm{Re}} \quad (4)$$

where Re is the Reynolds number. Eq. (4) is valid if the gas flow inside the capillary is laminar, which was the case for all the performed permeation experiments. The local oxygen partial pressure in the permeate side of the capillary P_2 can be expressed as [36]:

$$\frac{P_2}{P_T} = \frac{N_{O_2}}{N_{O_2} + N_{Ar}} \quad (5)$$

where N_{O_2} and N_{Ar} are the molar flow rates of the oxygen permeated to the permeate side of the capillary and the argon at the permeate side, respectively. Using Eq. (1), the values of $C_i D_a$ were calculated from the average p'_{O_2} and p''_{O_2} values. The measured oxygen fluxes were obtained from four-end lab-scale experiments at 750–950 °C (see Section 2.1). The obtained $C_i D_a$ value at 850 °C was then used for the numerical integration of Eq. (1) which required the capillary to be divided into 1000 equal segments. f, ρ, v, N_{O_2}, N_{Ar}, P_T and p''_{O_2} were calculated for each segment and the average oxygen flux through the capillary was calculated as:

$$j(O_2) = \frac{N_{O_2(out)}}{S} \quad (6)$$

where $N_{O_2(out)}$ is the molar flow rate of oxygen at the outlet of the permeate side of the capillary. The $C_i D_a$ value at 850 °C reveals the impact of the outer and inner diameter and total membrane length on the oxygen flux through a capillary membrane operating under power plant conditions.

2.3.2. Three-end integration mode

As oxygen is the only gas leaving the core side of the capillary in the three-end integration mode, the total pressure drop on the permeate side of the capillary dP_T

over an infinitesimal length dl equals dP_2:

$$dP_T = \frac{dP_2 = f\rho V^2}{2d} dl \quad (7)$$

As in Section 2.3.1, Eqs. (1) and (2) were used to calculate the local oxygen flux $j(O_2)_L$ limited by bulk diffusion and the effective membrane surface area dS over an infinitesimal length dl. The numerical integration of equation Eq. (1) was performed by dividing the capillary into 1000 equal segments and by calculating f, ρ, V and P_2 for each segment. The value of C_iD_a was obtained at 850 °C under four-end lab-scale conditions. The average oxygen flux through the capillary was calculated using Eq. (6), allowing us to assess the impact of the capillary geometry on its performance under power plant conditions.

3. Results and discussion

3.1. Modeling of the oxygen flux through sulfur-free BSCF capillaries measured under lab-scale conditions

Fig. 2 plots both the measured and modeled oxygen flux through a sulfur-free BSCF capillary against the argon sweep gas flow rate for temperatures between 750 and 950 °C. The model, which is based on bulk-diffusion limitation of the oxygen flux, shows generally good agreement with the experimental values. The corresponding C_iD_a values are listed in Table 1. However, at temperatures < 850 °C, the measured oxygen fluxes are found to be nearly independent of the sweep gas flow rate (> 70 Nml min^{-1}), indicating the presence of surface exchange kinetics limitations.

The authors [30] found in a previous report that the sulfur-free capillary membrane under investigation had an activation energy of 60 kJ/mol at temperatures between 750 and 850 °C, whereas at temperatures between 850 and 950 °C an activation energy of 39 kJ/mol was obtained. The latter energy is comparable to the activation energy of pure bulk diffusion through the BSCF membrane[38–40]. These results correspond well with the modeling results which indicate strong bulk diffusion limitation of the

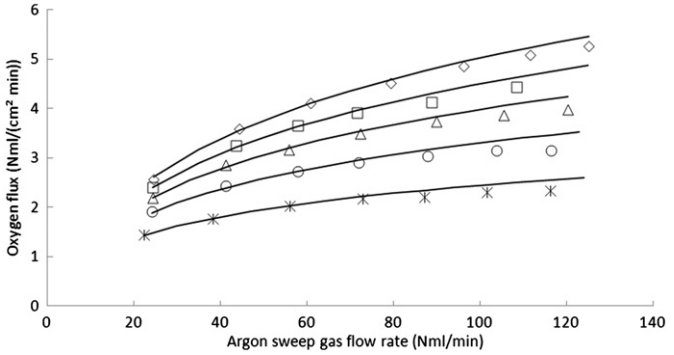

Fig. 2. Typical dependency of the oxygen permeation flux through a sulfur-free BSCF capillary on the Argon sweep gas flow rate at temperatures between 750 and 950 °C (750 °C (*), 800 °C (O), 850 °C (△), 900 °C (□) and 950 °C (◇)) together with the values obtained by the bulk diffusion limited model (solid lines).

Table 1
Modeling results of the oxygen permeation for sulfur-free BSCF capillaries.

T (°C)	C_iD_a (10^{-7} mol cm^{-1} s^{-1})
950	3.48 ± 0.10
900	2.92 ± 0.09
850	2.41 ± 0.06
800	1.81 ± 0.08
750	1.17 ± 0.04

oxygen flux at 850–950 °C. The C_iD_a value at 850 °C was used to assess the impact of the geometry on the performance of MIEC capillary membranes operating in the four- or three-end mode under industrially relevant conditions. This temperature was chosen due to it being the lowest temperature at which surface exchange kinetics limitations are no longer present.

3.2. Four-end integration of MIEC capillaries with a wall thickness of 0.4 mm

3.2.1. MIEC capillaries with D=0.34 cm and d=0.26 cm

The variation along the membrane of the total pressure P_T, the oxygen partial pressure P_2 and the total gas velocity V through the core side of a capillary are presented in Fig. 3 for different membrane lengths, along with the variation of the local oxygen flux through the membrane with an outer diameter (D) of 0.34 cm and an inner diameter (d) of 0.26 cm.

The results show that the total pressure P_T decreases along the membrane (total pressure drop) and that this drop increases with increasing membrane lengths. However, the drop is relatively small with a maximum value of ~3% for a membrane length of 60 cm. This indicates that the P_2 value in the core side of the capillary is mostly determined by the oxygen flow rate through the membrane at a certain dl and the oxygen flow rate upon entering the dl (Eq. (5)). The increase in the total pressure drop with increasing membrane lengths can be explained by the substantial drop in total gas velocity according to Eq. (3) (see Fig. 3B).

For all membrane lengths, the gas velocity leaving the core side of the capillary was fixed at 25 m s^{-1} (Fig. 3B). As the amount of oxygen produced in a capillary typically increases with increasing membrane length, the velocity of the sweep gas entering the core side of the capillary decreases with increasing total membrane length until it reaches a gas velocity of 25 m s^{-1} at the outlet of the core side of the membrane (Fig. 3B). At a fixed position x inside the membrane, the gas velocity decreases with increasing total membrane lengths. Thus, the outflow speed of oxygen decreases, increasing P_2 and decreasing the local oxygen flux. P_2 values, gas velocities V and local oxygen fluxes for fixed membrane positions of 1, 10 and 20 cm are shown in Table 2 for different total membrane lengths. The changes

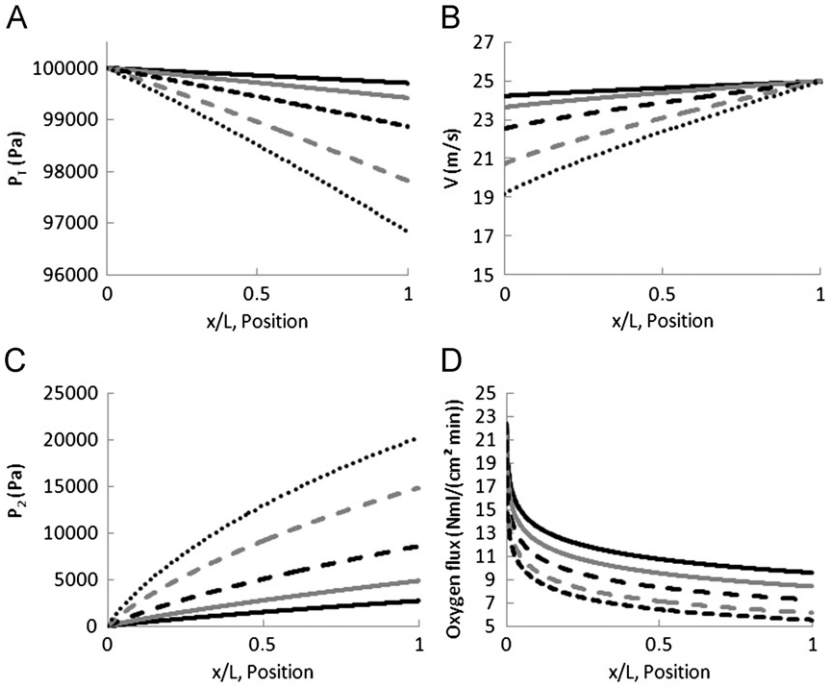

Fig. 3. Variation along the membrane of the total pressure P_T (A), total gas velocity V (B) and oxygen partial pressure P_2 (C) in the core side of a capillary together with the variation of the local oxygen flux through the membrane (D) with outer diameter $D=0.34$ cm and inner diameter $d=0.26$ cm for different membrane lengths (5 cm (solid black), 10 cm (solid gray), 20 cm (striped black), 40 cm (striped gray) and 60 cm (dotted black)).

Table 2
P_2 values, gas velocities V and local oxygen fluxes for fixed membrane positions x of 1, 10 and 20 cm for different total membrane lengths L.

L (cm)	pO_2 (Pa)	V (m s^{-1})	Flux (N ml cm^{-2} min^{-1})
$x=1$			
5	705	24.4	12.4
10	721	23.8	12.3
20	754	22.7	12.2
40	816	20.9	12.1
60	896	19.3	11.9
$x=10$			
10	4897	25.0	8.4
20	5088	23.9	8.4
40	5442	22.0	8.2
60	5809	20.4	8.1
$x=20$			
20	8625	25.0	7.3
40	9190	23.1	7.2
60	9773	21.4	7.0

in P_2 and oxygen flux are more pronounced at positions closer to the sweep side inlet due to the larger difference in V with increasing total membrane length.

As can be seen from Fig. 3C, P_2 typically increases along the membrane at fixed total membrane lengths due to the larger amount of oxygen in the core side of the capillary. Higher P_2 values are obtained for longer membranes due to the larger amount of oxygen being permeated through the membrane. Likewise, for fixed membrane positions x,

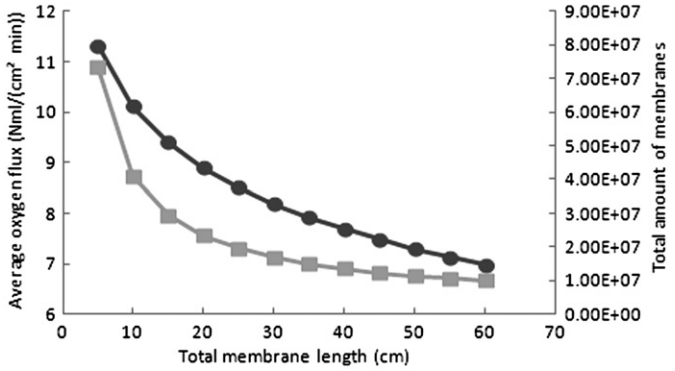

Fig. 4. Calculated average oxygen flux (circles) through the capillary membrane with $D=0.34$ cm and $d=0.26$ cm and the total number (squares) of membranes needed to produce 8000 TPD of oxygen for different total membrane lengths.

higher P_2 values are obtained for greater total membrane lengths due to the lower gas velocity at which the oxygen is swept through the core side (Table 2). Thus, the local oxygen flux decreases along the membrane due to a lower pO_2 gradient across the membrane wall (Fig. 4D). For fixed membrane positions x and increasing total membrane lengths, the larger the decrease in oxygen flux is, the lower the V values and the higher the P_2 values. This decrease in oxygen flux is most pronounced close to the sweep gas inlet ($x=1$ cm) due to the extremely low amount of oxygen in the sweep gas (5 Pa) (see Table 2).

The average oxygen flux through the capillary membrane is shown in Fig. 4. As can be seen clearly, the oxygen

flux decreases due to a lower pO_2 gradient across the membrane wall. As an example, for a membrane length of 40 cm, an average oxygen flux of 7.7 N ml cm^{-2} min^{-1} can be obtained at a fixed membrane thickness of 0.4 mm. In order to be commercially viable, fluxes need to be larger than 10 N ml cm^{-2} min^{-1} which can only be achieved by membrane lengths ≤ 10 cm at this membrane thickness.

The total number of membranes needed to produce 8000 t of oxygen per day (TPD) for different total membrane lengths is shown in Fig. 5 too. Due to the higher oxygen flow rate leaving the membrane at longer lengths, the total number of membranes typically decreases with greater total membrane lengths. At the same time, the required membrane surface area increases with increasing total membrane length due to the lower average oxygen flux. So, for a total membrane length of 40 cm a total number of $\sim$13.5 million membranes or a membrane surface area of $\sim$50500 m^2 is needed to produce 8000 t of oxygen per day. Around 41 million membranes or a membrane surface area of $\sim$38400 m^2 would be needed to produce the same amount of oxygen using a membrane length of only 10 cm.

3.2.2. MIEC capillaries with a fixed wall thickness of 0.4 mm and total membrane length of 30 cm

Fig. 5 shows the impact of decreasing outer and inner diameters on P_T, P_2, V and the oxygen flux along the membrane for a constant wall thickness of 0.4 mm and total membrane length of 30 cm.

P_T decreases along the membrane, but much more so with smaller outer and inner diameters (Fig. 5A). This decrease can be explained by the gas velocity profiles as presented in Fig. 5B. The total flow rate leaving the capillary decreases with decreasing inner diameters because, as already noted, for each membrane the gas velocity leaving the capillary is fixed at 25 m s^{-1}. Therefore, the sweep gas flow rate entering the capillary also decreases with decreasing diameter, leading to lower sweep gas velocities (Fig. 5B). Since ΔP_T increases with the increasing gas velocity and smaller inner diameters (Eq. (3)), larger total pressure drops are obtained for decreasing inner diameters. The lower gas velocities for smaller inner diameters also lead to increasing P_2 values along the membrane for smaller inner diameters since oxygen is swept away at lower velocities (Fig. 5C).

The faster stabilization of higher P_2 values at smaller inner diameters can be explained by a stronger decrease in total pressure and an almost linear increase of the gas velocity (and oxygen flow rate) (Eq. (5)). The increase in P_2 values with decreasing inner diameter leads to lower local oxygen fluxes with decreasing inner diameter due to the lower pO_2 gradient across the membrane (Fig. 5D). For a fixed outer and inner diameter, P_2 increases and the oxygen flux decreases along the membrane due to an increase of the oxygen content in the core side of the capillary.

3.2.3. MIEC capillaries with a fixed wall thickness of 0.4 mm and different outer diameters

In Fig. 6A the average oxygen flux through the capillary membranes is plotted against the total membrane length. As stated before, for a fixed outer and inner diameter the flux typically decreases with increasing length due to a higher amount of oxygen in the core side of the capillary.

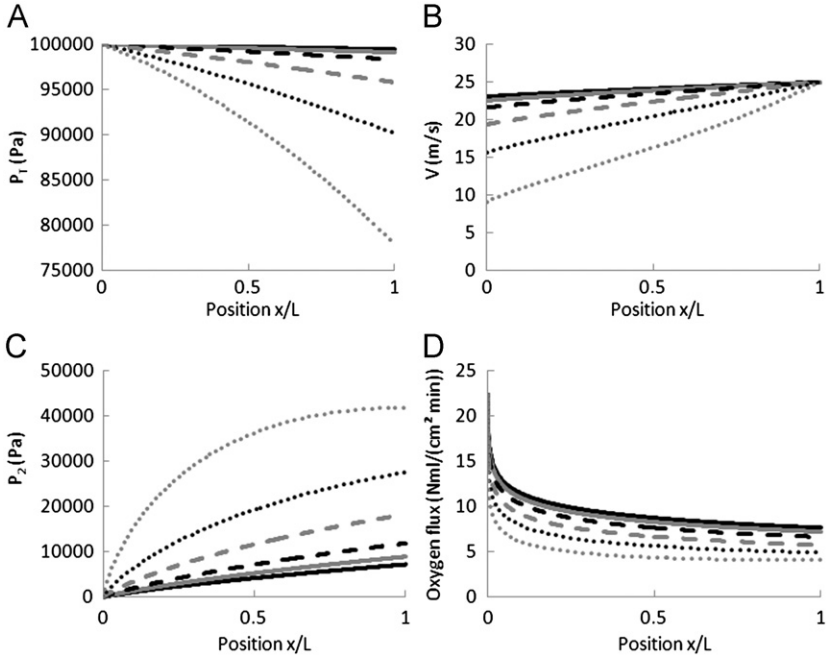

Fig. 5. Impact of decreasing outer and inner diameter (D_0=0.54 cm (solid black), 0.44 cm (solid gray), 0.34 cm (stripped black), 0.24 cm (stripped gray), 0.18 cm (dotted black) and 0.14 cm (dotted gray)), while retaining a constant wall thickness of 0.4 mm and a total membrane length of 30 cm, on P_T (A), V (B), P_2 (C) and oxygen flux (D) along the membrane.

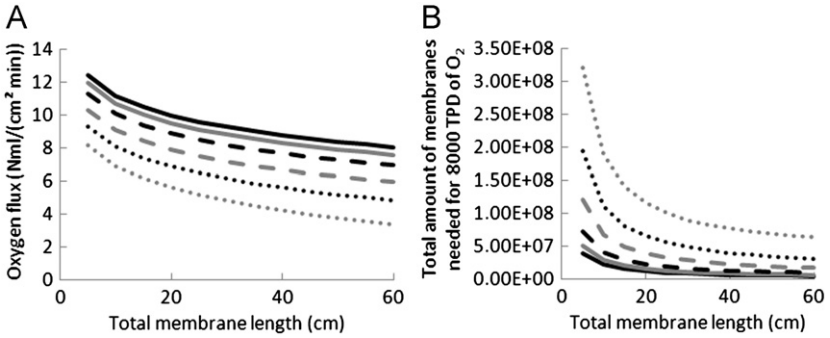

Fig. 6. Average oxygen flux (A) and the total number of membranes required to produce 8000 TPD of oxygen (B) at different total membrane lengths for decreasing inner diameters and a constant wall thickness of 0.4 mm. (D_0=0.54 cm (solid black), 0.44 cm (solid gray), 0.34 cm (striped black), 0.24 cm (striped gray), 0.18 cm (dotted black) and 0.14 cm (dotted gray)).

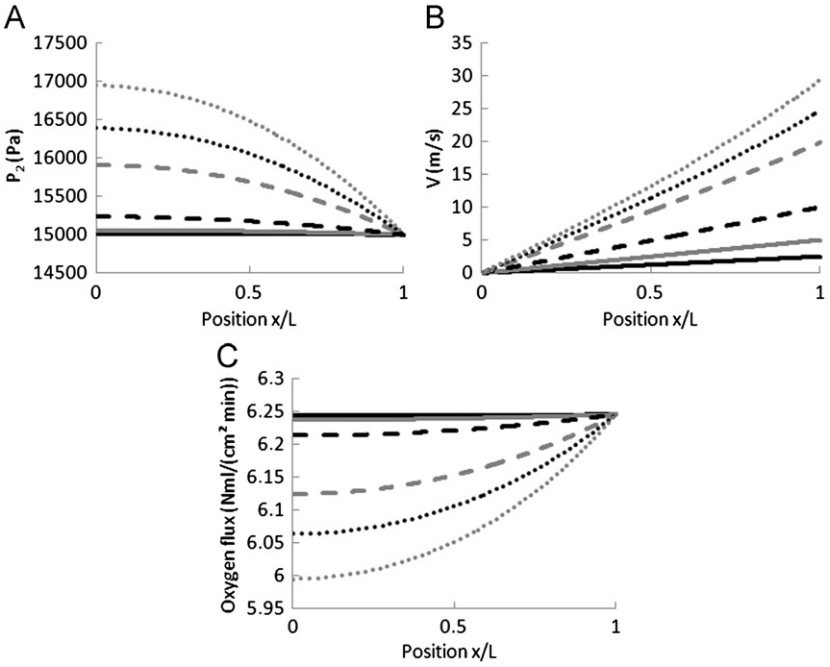

Fig. 7. Variation along the membrane of the total oxygen pressure P_2 (A) and the oxygen velocity V in the core side of a capillary (B) with outer diameter D=0.34 cm and inner diameter d=0.26 cm for different membrane lengths, [5 (solid black), 10 (solid gray), 20 (stripped black), 40 (stripped gray), 50 (dotted black) and 60 cm (dotted gray)] together with the variation of the local oxygen flux through the membrane (C).

The average oxygen flux also decreases with decreasing inner diameter due to the much higher P_2 inside the capillary caused by the lower sweep gas velocities. Therefore, much higher oxygen flow rates are obtained from capillaries with increasing inner diameters for fixed total membrane lengths.

The total number of membranes needed to produce 8000 TPD of oxygen are shown in Fig. 6B. Typically, the number of membranes decreases with greater total membrane length (and higher oxygen flow rate) and increases with smaller diameter for a fixed membrane length due to a lower oxygen flow rate leaving the capillary. So, it is questionable if using capillaries with smaller outer and inner diameters is beneficial for a four-end mode integration because, although decreasing diameters allows for higher surface to volume ratios, decreasing diameters require more membranes due to the lower average oxygen flux.

3.3. Three-end integration of MIEC capillaries with a wall thickness of 0.4 mm

3.3.1. MIEC capillaries with D=0.34 cm and d=0.26 cm

The plots in Fig. 7 illustrate the variation of total oxygen pressure P_2 (pO_2) and oxygen velocity V in the core side of a capillary with outer diameter D=0.34 cm and inner diameter d=0.26 cm for different membrane lengths, together with the variation of the local oxygen flux through the membrane.

The pO_2 in the core side decreases along the membrane length from the closed end side to the vacuum-pump side. This drop is more significant at greater total membrane

lengths (Fig. 7A). This decrease in pO_2 can be explained by the oxygen velocity profile along the membrane. For all total membrane lengths at the closed end of the capillary, the oxygen velocity is close to zero. However, at the vacuum end, a certain amount of oxygen is pumped away creating an oxygen flow rate. Therefore, at fixed membrane lengths, the application of a vacuum at the open end of the capillary leads to an increase in oxygen velocity (and thus oxygen flow rate) along the membrane from the closed end towards the end attached to the vacuum pump, This decreases the pO_2 in the core side of the capillary as that's where oxygen gets pumped out being pumped out at a far more rapid rate (Fig. 7A,B). In this way, for a fixed total membrane length, higher local oxygen fluxes are obtained closer to the vacuum side due to decreasing pO_2 (Fig. 7C). A larger increase of pO_2 and larger decrease in local oxygen flux towards the closed end of the capillary is obtained at higher total membrane lengths due to higher oxygen flow rate leaving the capillary and hence larger decrease of the oxygen velocity along the membrane towards the closed end (see Fig. 7A–C). In Table 3, pO_2 values, oxygen velocities V and local oxygen fluxes for fixed membrane positions of 1, 10, and 20 cm are shown for different total membrane lengths. Since the oxygen velocity for a fixed membrane position x and fixed applied vacuum decreases with increasing total membrane length, a higher pO_2 and lower local oxygen flux is obtained with the slower evacuation of the oxygen out of the core side of the capillary. Compared to the four-end integration mode, the drops in pO_2 and local oxygen flux are much smaller, ensuring more stable membrane operation due to the much smaller difference in chemical expansion along the capillary.

The average oxygen flux through the capillary membrane is shown in Fig. 8. It barely decreases with increasing total membrane length owing to the slightly higher pO_2 values in the core side of the capillary. Hence, an average oxygen flux

Table 3
pO_2 Values, oxygen velocities V and local oxygen fluxes for fixed membrane positions x of 1, 10, and 20 cm for different total membrane lengths L.

L (cm)	pO_2 (Pa)	V (m s^{-1})	Flux (N ml cm^{-2} min^{-1})
$x=1$			
5	15014	0.504	6.24
10	15059	0.503	6.24
20	15235	0.498	6.21
40	15910	0.475	6.12
60	16946	0.449	6.00
$x=10$			
10	15001	5.03	6.25
20	15177	4.96	6.22
40	15856	4.68	6.13
60	15896	4.32	6.00
$x=20$			
20	15000	10.03	6.25
40	15689	9.47	6.15
60	16742	8.68	6.02

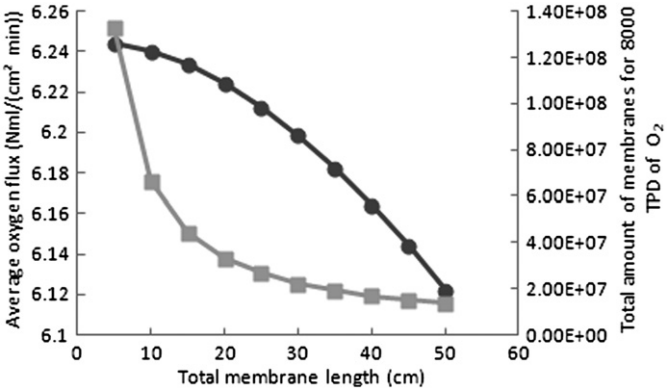

Fig. 8. Average oxygen flux (circles) through the capillary membrane with $D=0.34$ cm and $d=0.26$ cm and the total number (squares) of membranes needed to produce 8000 TPD of oxygen for different total membrane lengths.

of 6.1–6.2 N ml cm^{-2} min^{-1} is obtained for total membrane lengths between 5 and 50 cm. In contrast to the four-end mode operation, no significant drop in oxygen flux occurs with greater membrane length on account of the much smaller drop in pO_2. Note that for an outer diameter of 0.34 cm and an inner diameter of 0.26 cm the total membrane length is limited to 50 cm since at this length the oxygen velocity leaving the core side is ~25 m/s. For a membrane length of 40 cm an average oxygen flux of ~6.2 N ml cm^{-2} min^{-1} is obtained which is ~19% lower than the flux obtained in the four-end mode.

The total number of membranes needed for the production of 8000 TPD of oxygen is also shown in Fig. 8. The total number of membranes typically decreases with increasing membrane length due to the higher oxygen flow rate. The required membrane surface, however, only slightly increases with increasing membrane length due to the limited decrease of the average oxygen flux (~0.1 N ml cm^{-2} min^{-1}). For a total membrane length of 40 cm, a total membrane area of ~63000 m^2 is required to deliver 8000 TPD of oxygen, which is ~25% higher compared to the four-end integration mode.

3.3.2. MIEC capillaries with a fixed wall thickness of 0.4 mm and total membrane length of 30 cm

The impact of decreasing outer and inner diameters on P_2 (pO_2), V and the oxygen flux along the membrane, while retaining a constant wall thickness of 0.4 mm and a total membrane length of 30 cm, are shown in Fig. 9.

The pO_2 in the core side decreases from the closed end side to the vacuum pump side along the membrane. This decrease is more pronounced with smaller outer and inner diameters (see Fig. 9A) which can be explained by the gas velocity profiles presented in Fig. 9B. A higher oxygen velocity leaving the capillary is obtained for capillaries with smaller inner diameters according to Eq. (7). A vacuum was applied to each of these membranes. As noted above, the oxygen velocity at the core side decreases from the vacuum end to the closed end reaching zero, increasing

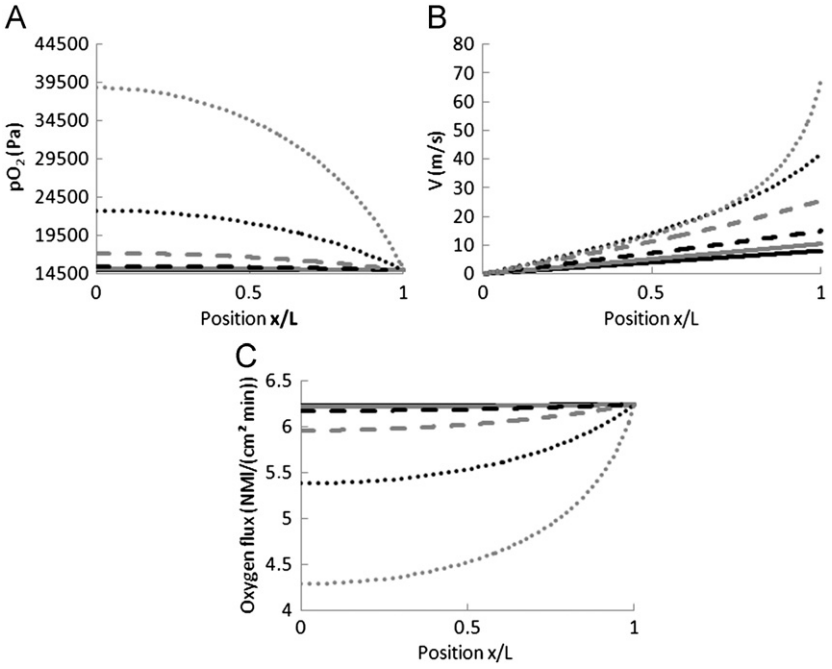

Fig. 9. Impact of decreasing outer and inner diameter, while retaining a constant wall thickness of 0.4 mm and a total membrane length of 30 cm, on pO_2 (A), V (B) and oxygen flux (C) along the membrane. (D_0=0.54 cm (solid black), 0.44 cm (solid gray), 0.34 cm (striped black), 0.24 cm (striped gray), 0.18 cm (dotted black) and 0.14 cm (dotted gray)).

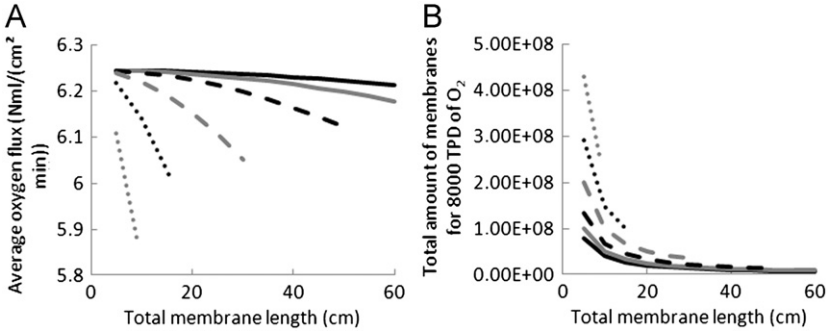

Fig. 10. Average oxygen flux (A) and the total (in square meters) of membranes (B) required to produce 8000 TDP of oxygen (B) at different total membrane lengths for decreasing inner diameters and a constant wall thickness of 0.4 mm. (D_0=0.54 cm (solid black), 0.44 cm (solid gray), 0.34 cm (striped black), 0.24 cm (striped gray), 0.18 cm (dotted black) and 0.14 cm (dotted gray)).

the pO_2 and decreasing the local oxygen flux along the membrane. In this way, largerer drops in oxygen velocity from the vacuum end to the closed end are obtained for capillaries with smaller inner diameters, leading to a larger increase in pO_2 and a larger decrease of the local oxygen fluxes towards the closed end (Fig. 9B–C). With the maximum allowable oxygen velocity leaving the capillary being 25 m s^{-1}, the maximum membrane length for an inner diameter of 0.26, 0.16, 0.1 and 0.06 cm are respectively 50, 30, 16 and 9 cm.

3.3.3. MIEC capillaries with a fixed wall thickness of 0.4 mm and different outer diameters

The average oxygen flux through the capillary membranes for different total membrane lengths is shown in Fig. 10A. As can be seen, the decrease of the oxygen flux with the total membrane length is more pronounced at smaller inner diameters due to the higher pO_2 values in the core side. However, compared to the four-end integration mode, the drop in oxygen flux results in only slightly more stable operation since large differences in chemical expansion along the membrane are avoided for total membrane lengths equal to or smaller than the maximum allowable length. For a total membrane length of ~10 cm and inner diameter of 0.06 cm, an average oxygen flux of ~5.9 N ml cm^{-2} min^{-1} is obtained in the three-end mode, whereas a flux of 6.9 N ml cm^{-2} min^{-1} is obtained in the four-end mode. For a total membrane length of 10 cm and an inner diameter of 0.26 cm, a flux of 6.2 N ml cm^{-2} min^{-1} is obtained in the three-end mode and a flux of 10.1 N ml

$cm^{-2}\,min^{-1}$ in the four-end mode. Therefore, the difference in oxygen flux between the three-end and four-end integration for similar length and diameter, decreases with smaller inner diameter due to a big increase in pO_2 for the four-end mode and a slight increase in pO_2 for the three-end mode.

The total number of membranes needed to produce 8000 TPD of oxygen is shown in Fig. 10B. Typically, the total number of membranes decreases with increasing membrane length due to the higher oxygen flow rates leaving the capillaries. Furthermore, the required membrane area slightly increases with increasing membrane length and with decreasing inner diameters due to a limited pO_2 drop in the core side. The total required membrane areas for a total membrane length of $\sim$10 cm and an inner diameter of 0.06 cm amounts to $\sim$66000 m^2 for the three-end mode and $\sim$56000 m^2 for the four-end mode. On the other hand, the required membrane area for a total membrane length of $\sim$10 cm and an inner diameter of 0.26 cm equals $\sim$62000 m^2 for the three-end mode and $\sim$38000 m^2 for the four-end mode.

4. Conclusions

In the work described herein, the performance of BSCF capillaries with a wall thickness of 0.4 mm was modeled under power plant conditions for both a three-end and four-end integration mode assuming bulk diffusion limitation of the oxygen flux and using parameters of sulfur-free BSCF capillaries derived from lab-scale experimental values. The modeling revealed that, in the four-end mode, higher average oxygen fluxes and smaller total membrane areas are obtained compared to the three-end mode. This is due to the higher pO_2 gradient across the membrane wall. However, the oxygen flux in the four-end mode markedly decreases with increasing total membrane length and decreasing inner diameters. This is due to the higher level of pO_2 in the core side of the capillaries, leading to larger total membrane areas and an oxygen flow rate of 8000 TPD. In the three-end mode, these drops in pO_2 are much less significant for total membrane lengths equal or smaller than the maximum permissible length which is determined by a maximum gas velocity of 25 m s^{-1} leaving the capillary. This leads to a much more stable operation since large differences in chemical expansion along the membrane are avoided. In the four-end mode the commercially interesting oxygen flux of 10 N ml $cm^{-2}\,min^{-1}$ could only be obtained for a minimum inner diameter of 1.6 mm even though membrane lengths that are suitable for module design would require an inner diameter >4.6 mm. In the three-end mode, an average oxygen flux of *ca.* 6 N ml $cm^{-2}\,min^{-1}$ can be achieved while the total membrane length of capillaries with inner diameters ≤ 1 mm is restricted to below 16 cm. These results indicate that, especially in the case of the three-end integration mode, capillaries with dense wall thicknesses <0.4 mm are necessary to achieve the desired oxygen flux of 10 N ml $cm^{-2}\,min^{-1}$. Such membranes with improved fluxes, consisting of a thin dense BSCF layer combined with a porous BSCF support layer, have recently been prepared by Han et al. [41].

Acknowledgments

The authors wish to thank all the VITO staff involved in the project for their continued support, and in particular B. Molenberghs, W. Doyen, H. Beckers and S. Mullens. C. Buysse would like to acknowledge funding from VITO and the University of Antwerp for a Ph.D. studentship. This work has been performed in the framework of the German Helmholtz Alliance Project "MEM-BRAIN", aiming at the development of gas separation membranes for zero-emission fossil fuel power plants.

References

[1] R. Castillo, Thermodynamic analysis of a hard coal oxyfuel power plant with high temperature three-end membrane for air separation, Applied Energy 88 (5) (2011) 1480–1493.
[2] C. Chen, E.S Rubin, CO_2 control technology effects on IGCC plant performance and cost, Energy Policy 37 (3) (2009) 915–924.
[3] K. Damen, M. van Troost, A. Faaij, W. Turkenburg, A comparison of electricity and hydrogen production systems with CO_2 capture and storage. Part A: review and selection of promising conversion and capture technologies, Progress in Energy and Combustion Science 32 (2) (2006) 215–246.
[4] H.M. Kvamsdal, K. Jordal, O. Bolland, A quantitative comparison of gas turbine cycles with CO_2 capture, Energy 32 (1) (2007) 10–24.
[5] H. Stadler, F. Beggel, M. Habermehl, B. Persigehl, R. Kneer, M. Modigell, P. Jeschke, Oxyfuel coal combustion by efficient integration of oxygen transport membranes, International Journal of Greenhouse Gas Control 5 (1) (2010) 7–15.
[6] S.G. Sundkvist, S. Julsrud, B. Viyeland, T. Naas, M. Budd, H. Leistner, D. Winkler, Development and testing of AZEP reactor components, International Journal of Greenhouse Gas Control 1 (2) (2007) 180–187.
[7] H.J.M. Bouwmeester, Dense ceramic membranes for methane conversion, Catalysis Today 82 (1–4) (2003) 141–150.
[8] R. Bredesen, K. Jordal, A. Bolland, High-temperature membranes in power generation with CO_2 capture, Chemical Engineering and Processing 43 (9) (2004) 1129–1158.
[9] P.N. Dyer, R.E. Richards, S.L. Russek, M. T.D., Ion transport membrane technology for oxygen separation and syngas production, Solid State Ionics 134 (1–2) (2000) 21–33.
[10] M.V. Mundschau, X. Xie, C.R. Evenson, A.F. Sammells, Dense inorganic membranes for production of hydrogen from methane and coal with carbon dioxide sequestration, Catalysis Today 118 (1–2) (2006) 12–23.
[11] J. Sunarso, S. Baumann, J.M. Serra, W.A. Meulenberg, S. Liu, Y.S. Lin, J. da Costa, Mixed ionic–electronic conducting (MIEC) ceramic-based membranes for oxygen separation, Journal of Membrane Science 320 (1–2) (2008) 13–41.
[12] R. Bredesen, J. Sogge, A technical and economic assessment of membrane reactors for hydrogen and syngas production, in: seminar on the ecological applications of innovative membrane technology in the chemical industry, Cetraro, Calabria, Italy, 1996.
[13] J.F. Vente, S. McIntosh, W.G. Haije, H.J.M. Bouwmeester, Properties and performance of $Ba_xSr_{1-x}Co_{0.8}Fe_{0.2}O_3$-delta materials for oxygen transport membranes, Journal of Solid State Electrochemistry 10 (8) (2006) 581–588.

[14] J. Caro, H.H. Wang, C. Tablet, A. Kleinert, A. Feldhoff, T. Schiestel, M. Kilgus, P. Kolsch, S. Werth, Evaluation of perovskites in hollow fibre and disk geometry in catalytic membrane reactors and in oxygen separators, Catalysis Today 118 (1–2) (2006) 128–135.
[15] M. Mulder, Basic Principles of Membrane Technology, 2nd Edition, Kluwer Academic Publishers, Dordrecht, The Netherlands, 1996.
[16] T. Schiestel, M. Kilgus, S. Peter, K.J. Caspary, H. Wang, J. Caro, Hollow fibre perovskite membranes for oxygen separation, Journal of Membrane Science 258 (1–2) (2005) 1–4.
[17] X.Y. Tan, Z.B. Pang, K. Li, Oxygen production using $La_{0.6}Sr_{0.4}Co_{0.2}Fe_{0.8}O_3$-alpha (LSCF) perovskite hollow fibre membrane modules, Journal of Membrane Science 310 (1–2) (2008) 550–556.
[18] E.M. Pfaff, A. Kaletsch, C. Broeckmann, Design of a mixed ionic/electronic conducting oxygen transport membrane pilot module, Chemical Engineering and Technology 35 (3) (2012) 455–463.
[19] A.A. Asadi, A. Behrouzifar, M. Iravaninia, T. Mohammadi, A. Pak, Preparation and oxygen permeation of $La_{0.6}Sr_{0.4}Co_{0.2}Fe_{0.8}O_3$-delta (LSCF) perovskite-type membranes: experimental study and mathematical modeling, Industrial and Engineering Chemistry Research 51 (7) (2012) 3069–3080.
[20] A. Behrouzifar, A.A. Asadi, T. Mohammadi, A. Pak, Experimental investigation and mathematical modeling of oxygen permeation through dense $Ba_{0.5}Sr_{0.5}Co_{0.8}Fe_{0.2}O_3$ (BSCF) perovskite-type ceramic membranes, Ceramics International 38 (6) (2012) 4797–4811.
[21] A. Ghadimi, M.A. Alaee, A. Behrouzifar, A.A. Asadi, T. Mohammadi, Oxygen permeation of $Ba_xSr_{1-x}Co_{0.8}Fe_{0.2}O_3$-delta perovskite-type membrane: experimental and modeling, Desalination 270 (1–3) (2012) 64–75.
[22] S. Engels, F. Beggel, M. Modigell, H. Stadler, Simulation of a membrane unit for oxyfuel power plants under consideration of realistic BSCF membrane properties, Journal of Membrane Science 359 (1–2) (2010) 93–101.
[23] S. Engels, T. Markus, M. Modigell, L. Singheiser, Oxygen permeation and stability investigations on MIEC membrane materials under operating conditions for power plant processes, Journal of Membrane Science 370 (1–2) (2011) 58–69.
[24] J.F. Vente, W.G. Haije, Z.S. Rak, Performance of functional perovskite membranes for oxygen production, Journal of Membrane Science 276 (1–2) (2006) 178–184.
[25] M. Arnold, T.M. Gesing, J. Martynczuk, A. Feldhoff, Correlation of the formation and the decomposition process of the BSCF perovskite at intermediate temperatures, Chemistry of Materials 20 (18) (2008) 5851–5858.
[26] M. Arnold, H.H. Wang, A. Feldhoff, Influence of CO_2 on the oxygen permeation performance and the microstructure of perovskite-type $(Ba_{0.5}Sr_{0.5})(Co_{0.8}Fe_{0.2})O_3$-delta membranes, Journal of Membrane Science 293 (1–2) (2007) 44–52.
[27] S. Svarcova, K. Wiik, J. Tolchard, H.J.M. Bouwmeester, T. Grande, Structural instability of cubic perovskite $Ba_xSr_xSr_{1-x}Co_{1-y}Fe_yO_3$-delta, Solid State Ionics 178 (35–36) (2008) 1787–1791.
[28] A.Y. Yan, L. Bin, Y.L. Dong, Z.J. Tian, D.Z. Wang, M.J. Cheng, A temperature programmed desorption investigation on the interaction of $Ba_{0.5}Sr_{0.5}Co_{0.8}Fe_{0.2}O_3$-delta perovskite oxides with CO_2 in the absence and presence of H_2O and O-2, Applied Catalysis B-Environmental 80 (1–2) (2008) 24–31.
[29] C. Buysse, A. Kovalevsky, F. Snijkers, A. Buekenhoudt, S. Mullens, J. Luyten, J. Kretzschmar, S. Lenaerts, Development, performance and stability of sulfur-free, macrovoid-free BSCF capillaries for high temperature oxygen separation from air, Journal of Membrane Science 372 (1–2) (2011) 239–248.
[30] J. Van Noyen, V. Middelkoop, C. Buysse, A. Kovalevsky, F.A. Snijkers, S. Buekenhoudt, J. Mullens, J. Luyten, S. Kretzschmar, Lenaerts, Fabrication of perovskite capillary membranes for high temperature gas separation, Catalysis Today 193 (2012) 172–178.
[31] C. Buysse, A. Kovalevsky, F. Snijkers, A. Buekenhoudt, S. Mullens, J. Luyten, J.L.S. Kretzschmar, Fabrication and oxygen permeability of gastight, macrovoid-free $Ba_{0.5}Sr_{0.5}Co_{0.8}Fe_{0.2}O_3$-delta capillaries for high temperature gas separation, Journal of Membrane Science 359 (1–2) (2010) 86–92.
[32] A. Kovalevsky, C. Buysse, F. Snijkers, A. Buekenhoudt, J. Luyten, J. Kretzschmar, S. Lenaerts, Oxygen exchange-limited transport and surface activation of $Ba_{0.5}Sr_{0.5}Co_{0.8}Fe_{0.2}O_3$-delta capillary membranes, Journal of Membrane Science 368 (1–2) (2011) 223–232.
[33] J.F. Vente, W.G. Haije, R. Ijpelaan, F.T. Rusting, On the full-scale module design of an air separation unit using mixed ionic electronic conducting membranes, Journal of Membrane Science 278 (1–2) (2006) 66–71.
[34] R. Kriegel, Efficient Oxygen Separation With the Help of Ceramic Membranes, Hannover Messe, Hannover, Germany, 2010.
[35] S. Liu, X. Tan, Z. Shao, J.C.D. da Costa, $Ba_{0.5}Sr_{0.5}Co_{0.8}Fe0_{.2}O_3$-delta ceramic hollow-fiber membranes for oxygen permeation, AIChE Journal American Institute of Chemical Engineers 52 (10) (2006) 3452–3461.
[36] H.H. Wang, R. Wang, D.T. Liang, W.S. Yang, Experimental and modeling studies on $Ba_{0.5}Sr_{0.5}Co_{0.8}Fe_{0.2}O_3$-delta (BSCF) tubular membranes for air separation, Journal of Membrane Science 243 (1–2) (2004) 405–415.
[37] S. Kim, Y.L. Yang, A.J. Jacobson, B. Abeles, Diffusion and surface exchange coefficients in mixed ionic electronic conducting oxides from the pressure dependence of oxygen permeation, Solid State Ionics 106 (3–4) (1998) 189–195.
[38] S. Baumann, F. Schulze-Kuppers, S. Roitsch, M. Betz, M. Zwick, E.M. Pfaff, W.A. Meulenberg, J. Mayer, D. Stover, Influence of sintering conditions on microstructure and oxygen permeation of $Ba_{0.5}Sr_{0.5}Co_{0.8}Fe_{0.2}O_3$-delta (BSCF) oxygen transport membranes, Journal of Membrane Science 359 (1–2) (2010) 102–109.
[39] Z.P. Shao, S.M. Haile, A high-performance cathode for the next generation of solid-oxide fuel cells, Nature 431 (7005) (2004) 170–173.
[40] L. Wang, R. Merkle, J. Maier, T. Acarturk, U. Starke, Oxygen tracer diffusion in dense $Ba_{0.5}Sr_{0.5}Co_{0.8}Fe_{0.2}O_3$-delta films, Applied Physics Letters 94 (7) (2009) 3.
[41] D. Han, X. Tan, Z. Yan, Q. Li, S. Liu, New morphological $Ba_{0.5}Sr_{0.5}Co_{0.8}Fe_{0.2}O_3$-$\alpha$ hollow fibre membranes with high oxygen permeation fluxes, Ceramics International (2012).